IOP Publishing Measurement Science and Technology
Meas. Sci. Technol. **31** (2020) 055401 (12pp) https://doi.org/10.1088/1361-6501/ab62c4

Electrical resistance tomography with conditional generative adversarial networks

Yutong Chen[1,2,4], **Kun Li**[1,3] and **Yan Han**[1]

[1] Shanxi Key Lab of Signal Capturing and Processing, North University of China, Taiyuan 030051, People's Republic of China
[2] Department of Electrical Engineering and Automation, Shanxi Polytechnic College, Taiyuan 030006, People's Republic of China
[3] School of Chemical and Process Engineering, University of Leeds, Leeds LS2 9JT, United Kingdom

E-mail: cyt_nuc@163.com (Y Chen)

Received 27 July 2019, revised 10 December 2019
Accepted for publication 17 December 2019
Published 31 January 2020

Abstract

Electrical resistance tomography (ERT) can reconstruct measured field images non-invasively and is therefore widely used in the field of engineering technology. However, blurred reconstructed images and the lack of detailed features limit the application of electrical tomography. In this paper, a reconstruction method based on a conditional generative adversarial network (CGAN) is proposed to mitigate these problems. CGAN, a deep learning algorithm, can generate images based on condition information, making the generated images more stable and trustable. To adapt the training to the characteristics of ERT, the CGAN structure has been improved. In addition, loss judgement is added to the discriminator training to improve the training efficiency. We further propose a data generation method to simulate various conductivity distributions. The method is tested by using a testing set without repetition data in the training set. The results indicate that the method can effectively improve the sharpness of the reconstructed images and the reconstruction of the image details and reduce reconstructed image error. Using real experimental data for reconstruction, the results also show that this method can effectively improve the quality of reconstruction.

Keywords: conditional generative adversarial network, deep learning, electrical resistance tomography, image reconstruction

(Some figures may appear in colour only in the online journal)

1. Introduction

Electrical resistance tomography (ERT) [1] is a kind of electrical tomography (ET) technology that reconstructs the conductivity distribution of the sensing domain through the measured boundary voltage [2]. ERT is widely applied for multi-phase flow processes [3], biomedical monitoring [4], etc, because it can non-intrusively visualize the domain.

Reconstruction of ERT is a severely ill-posed nonlinear inverse problem. The reconstructed image of ERT usually suffers from distortion and low resolution. To improve image quality, algorithms such as the sensitivity coefficient back projection (SBP) method [5], Tikhonov algorithm [6], Newton–Raphson algorithm [7], and iterative Landweber algorithm [8] have been proposed. These reconstruction algorithms greatly improve the image quality. However, blurred reconstructed images and the lack of detailed features remain key factors that restrict the application of ERT.

In recent years, deep learning has flourished in image processing. Because deep learning techniques are good at mapping complicated nonlinear functions, deep learning has recently been introduced into ET reconstruction. An

[4] Author to whom any correspondence should be addressed.

autoencoder neural network has been employed in electrical capacitance tomography (ECT) [9]. Convolutional neural networks (CNNs) have been used in electrical impedance tomography (EIT) [10] and ERT [11]. Two deep learning image reconstruction algorithms have been used in electrical tomography [12]. A new cost function for ECT has been proposed [13]. Improving the quality of image reconstruction by using deep learning techniques has become an important direction of ERT research. As a deep learning technique, conditional generative adversarial networks (CGANs) [14] can generate images based on provided information, which renders the image generation process controlled, and can effectively improve the detailed features of the generated image. Due to these characteristics, CGANs have attracted widespread attention in the field of image processing [15–17].

In this paper, we analyse the seriously ill-posed problem of ERT image reconstruction and propose a deep learning structure based on a CGAN to estimate high-quality reconstructed ERT images from severely distorted images. The generator and discriminator are important components in a CGAN, and the difficulty of discrimination increases with improvements in the generation ability. Therefore, in this paper, the loss of the discriminator is used as the basis for setting the training times of the discriminator. Furthermore, a data generation method is proposed to simulate various conductivity distributions. Experimental data from a practical ERT system are used to verify the practicability of the structure.

2. ERT reconstruction based on a CGAN

2.1. Principles of ERT reconstruction

A typical ERT system is shown in figure 1. A current is injected into a pair of adjacent electrodes, and the voltages between the remaining pairs of adjacent electrodes are measured. When the field conductivity is perturbed, the measured boundary voltage will change accordingly. ERT can reconstruct the field from the change in boundary voltage.

When the perturbation is small, based on the sensitivity coefficient principle, the conductivity distribution can be reconstructed by using the sensitivity matrix principle.

However, the reconstructed image will produce large errors when the perturbation is great. Therefore, in this paper, the reconstructed image is selected as the initial image, and a deep learning method is used to improve the accuracy of the reconstructed image.

2.2. CGAN structure for ERT image reconstruction

As shown in figure 2, the network structure consists of two modules: a preprocessing module and a deep learning module.

In the preprocessing module, the measured voltage is reconstructed into the conductivity image by inversion algorithms.

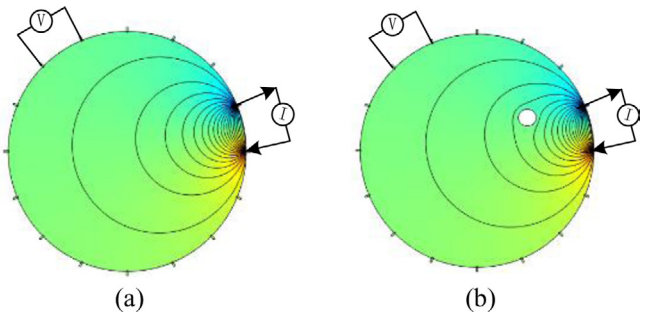

Figure 1. The 16-electrode ERT model. (a) Uniform conductivity. (b) Perturbed conductivity.

The conductivity image is employed as the input of the deep learning module.

The goal of the deep learning module is to map the initial image to the real image. x denotes the initial image, and y denotes the condition, which is the real conductivity distribution image. G denotes the generator, and D denotes the discriminator. G generates the image $G(x, z)$ according to the initial image x and the random noise z. The goal of G is to bring $G(x, z)$ as close to y as possible: $G : \{x, z\} \rightarrow y$. Then, x is combined with $G(x, z)$ and y and input to the discriminator D for discrimination, respectively. D is trained to discriminate these two groups of combinations. If the input is a combination of x and $G(x, z)$, then the output of D should be 'Fake'. If the input is a combination of x and y, then the output of D should be 'Real'. In the CGAN algorithm, 'Fake' and 'Real' are distinguished by the output value. Both G and D can be nonlinear mapping functions [14].

The training process of the deep learning module in this paper is shown in figure 3. G denotes a generator, and D denotes a discriminator. *Cycle* represents the number of training cycles for G and D, and K represents the maximum value of the training cycles. *T_g* and *T_d* represent the training times of G and D, respectively, in each cycle. M and N are the maximum values of *T_g* and *T_d*, respectively. $L_{\mathrm{CGAN}}(D)$ is the loss of D during training, and μ is a threshold near 0.

First, G is trained M times. Then, if the training cycle is less than K, D is trained. To improve the training efficiency, D is trained a number of times that varies with the loss of D. In this paper, $L_{\mathrm{CGAN}}(D)$ is used as the basis for setting the number of times that D is trained. If $L_{\mathrm{CGAN}}(D) < \mu$, D is considered to be capable of distinguishing between two combinations. Then, training of D is stopped, and G is trained. To avoid training D in an infinite loop, we set the maximum number of times that D is trained (N) in each training cycle. If D cannot distinguish the two combinations after N training times in each cycle, then the training of D is stopped, and G is trained. If the training cycle reaches K, then the training of the CGAN is stopped.

During training, G will be trained K cycles, while D will be trained $\mathrm{K} - 1$ cycles. After training is completed, in the actual application, only G is reserved for image generation, and D is no longer used.

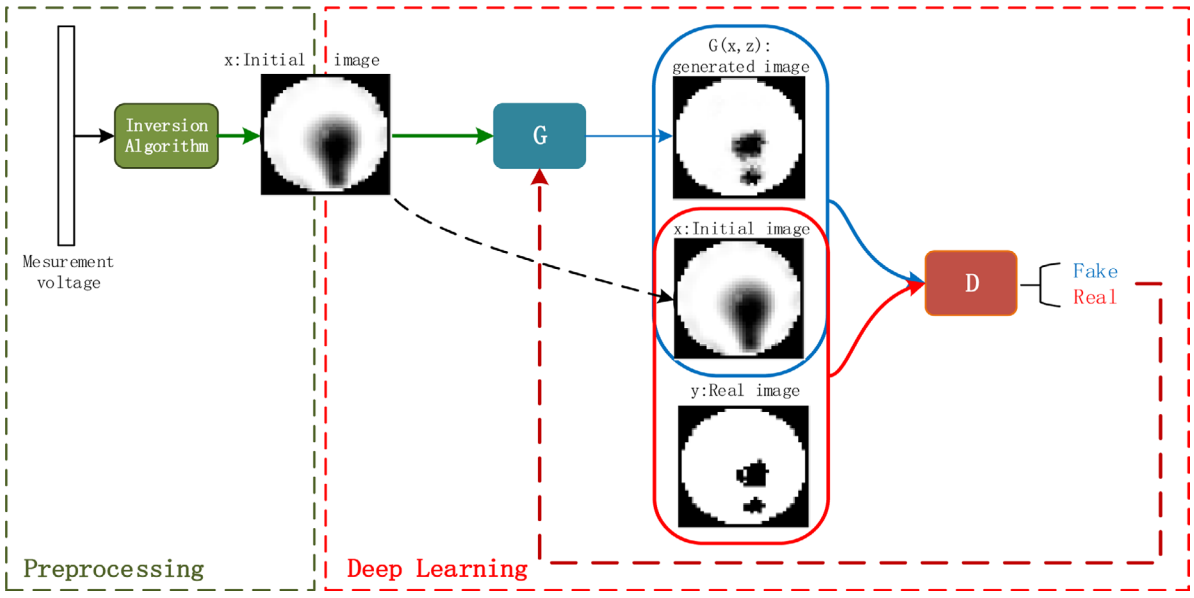

Figure 2. CGAN structure for ERT image reconstruction.

2.3. Details of G and D

Because of excellent performance in image processing, the CNN is used as the generator in this paper, as shown in figure 4. The kernel of the convolutional layer is 3×3. The size of the input image is 36×36. LeakyReLU is chosen as the activation function in the front layers, and Tanh is chosen in the last layer.

The function of D is to distinguish between the combination of the initial image x and the real image y and the combination of the initial image x and the generated image $G(x, z)$. The structure of D is shown in figure 5, and CNN is also adopted. In this paper, D has two convolutional layers and three fully connected layers. The kernel of the convolutional layer is 5×5. Sigmoid is chosen in the last layer to map the entire real interval to the (0, 1) interval. The output of training should be near 0 when the input is a combination of x and $G(x, z)$, and the output should be near 1 when the input is a combination of x and y.

2.4. Objective

The objective of this paper can be expressed as [14, 15]

$$G^* = \arg\min_G \max_D L_{\mathrm{CGAN}}(G, D) + \lambda L_{L1}(G)$$
$$\begin{cases} L_{CGAN}(G, D) = E_{x,y}\left[\log D(x, y)\right] \\ +E_{x,z}\left[\log(1 - D(x, G(x, z))\right] \\ L_{L1}(G) = E_{x,y,z}\left[\|y - G(x, z)\|_1\right], \end{cases} \tag{1}$$

where λ is the weighting term to balance the losses. $L_{\mathrm{CGAN}}(G, D)$ is the objective of the CGAN, where G tries to minimize this objective, and D tries to maximize it. For industrial monitoring, the trustworthiness of the generated image is very important. Therefore, the pixel-wise loss $L_{L1}(G)$ is adopted to bring the generated image closer to the real image. Since the output range of D is (0, 1), all items in the logarithm are positive.

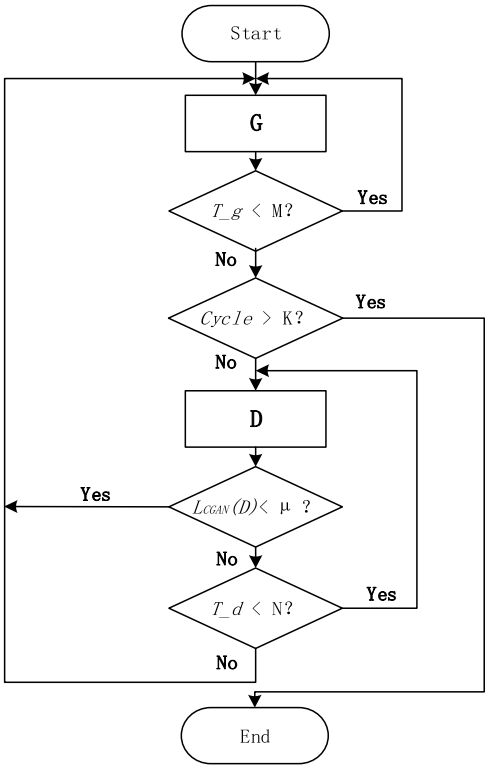

Figure 3. Training process.

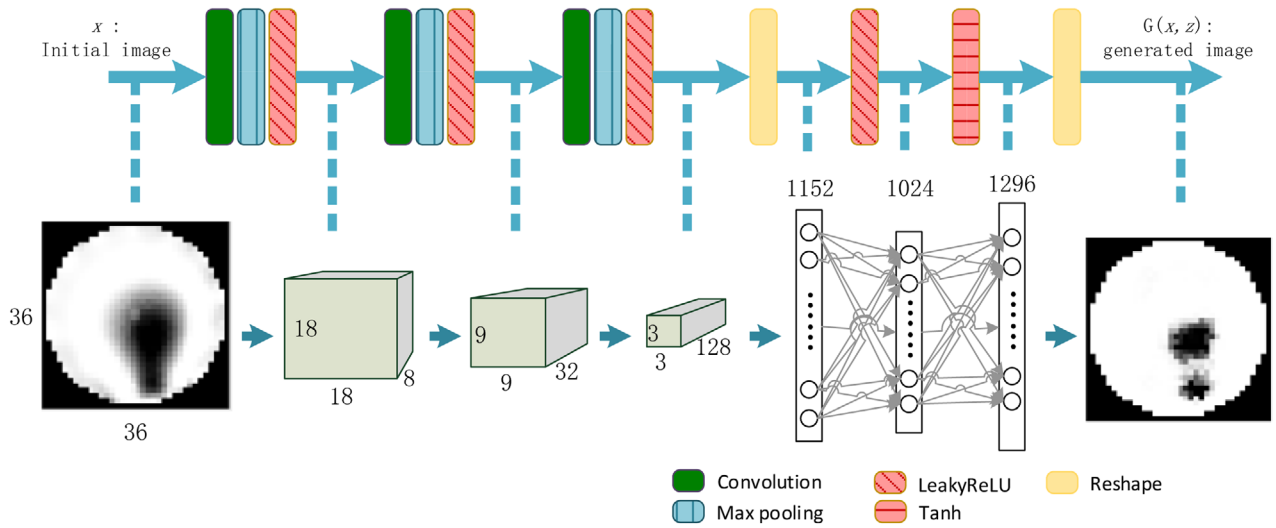

Figure 4. Generator of the CGAN.

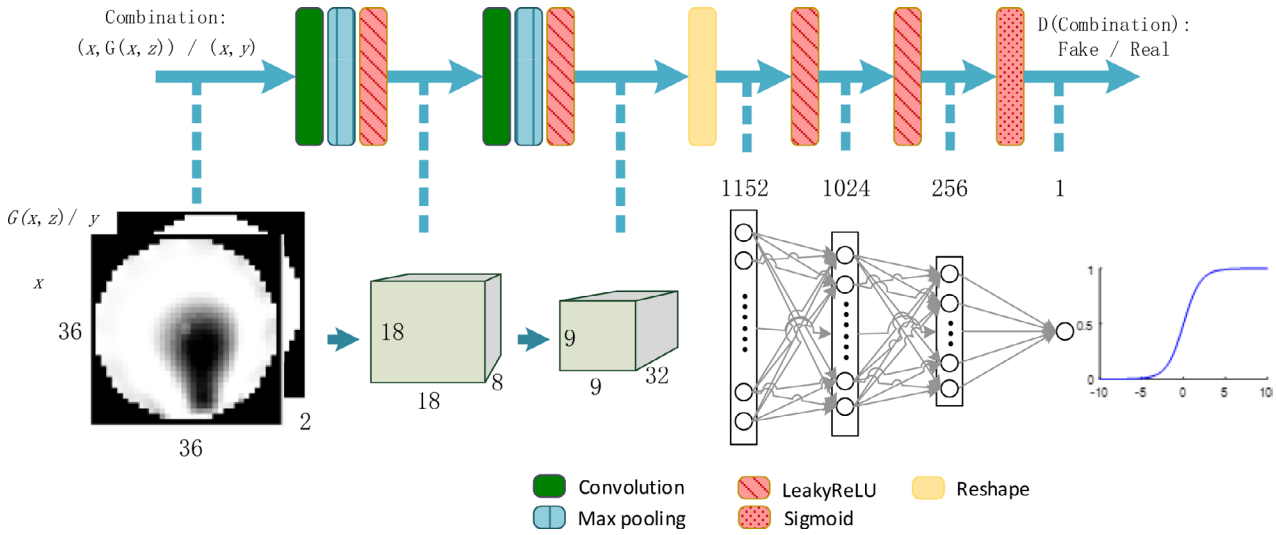

Figure 5. Discriminator of the CGAN.

In this paper, the training objectives G and D can be mathematically expressed as follows:

$$L_{\mathrm{CGAN}}(G) = \min_{G} \left[\log(1 - D(x, G(x, z))) + \log \|y - G(x, z)\|_1\right] \tag{2}$$

$$L_{\mathrm{CGAN}}(D) = \min_{D} \left[-\left[\log D(x, y) + \log(1 - D(x, G(x, z))\right]\right]. \tag{3}$$

3. Experimental method

3.1. Datasets

In the ERT image, the field space is divided into 1296 pixels, as shown in figure 6. The concerned domain of interest is within the circle.

Data sets are very important for deep learning, as the neural network will learn a distribution from them and generalize data sets. The more comprehensive the data simulation, the stronger the generalization performance of the model after training. In practical applications, a gas–liquid distribution is diverse. To simulate the diversity of the distribution, we randomize the gas distribution in this paper. The data generation process is shown in figure 7, and it is performed by using MATLAB.

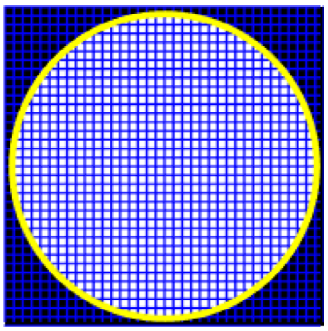

Figure 6. Mesh grid.

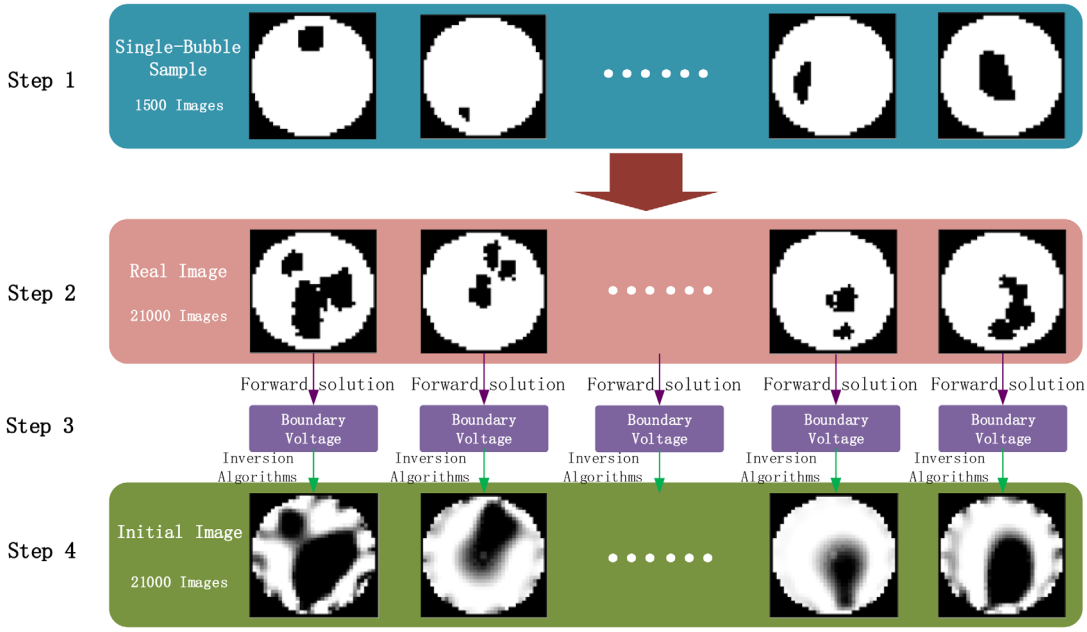

Figure 7. Data set for deep learning.

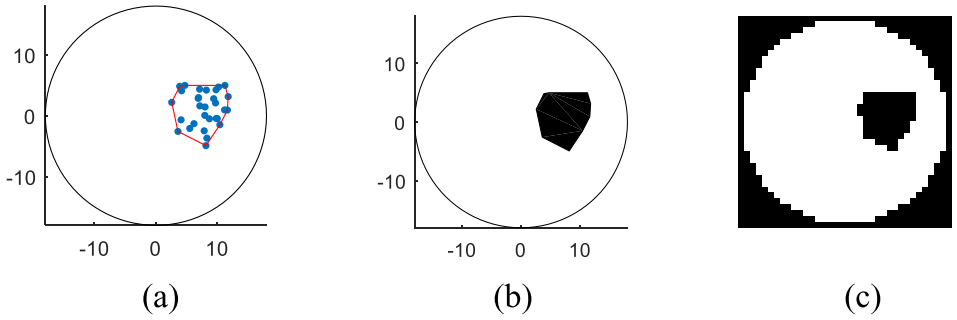

Figure 8. Generation of single bubble. (a) Generation of discrete points. (b) Single bubble image. (c) 36 ∗ 36 pixel image.

Step 1: Single-bubble samples of distribution are randomly generated in the domain. A single-bubble sample is a sample with only one bubble in each distribution, and the conductivity $\sigma = 0$ in the bubble. The generation process of a single bubble image is shown in figure 8.

To simulate a single bubble with different shapes, sizes, and locations, discrete points are generated and surrounded, as shown in figure 8(a). The conductivity in the enclosed range is set to 0 to generate a single bubble, as shown in figure 8(b). The single bubble image is converted into a 36 ∗ 36 pixel conductivity distribution image, as shown in figure 8(c). Field radius is assumed to be 15, the distance between the bubble centre and the region centre obeys an even distribution over the interval [2, 10]. The number of discrete points to form a bubble obeys an even distribution over the interval [30, 60]. Considering the factor of image resolution, excessively large and small bubbles are abandoned, and only the suitable bubbles are adopted to combine into a complex gas distribution. The radius of single bubbles obeys a normal distribution over the interval [2, 10] with a mean of 3 and a variance of 1.

Step 2: W samples are randomly extracted from step 1 for combination. In this paper, 21 000 complex distribution images are combined as the real image y. Their positions are determined by step 1. W is a number that obeys an even distribution over the internal [1, 9], to form a variety of complex distributions.

Step 3: A total of 21 000 sets of boundary voltage measurements of the field are obtained by a positive problem algorithm.

Step 4: An inversion algorithm is used to reconstruct the conductivity distribution. The reconstructed image is used as the initial image x for deep learning. In this paper, we use the Landweber algorithm and Newton–Raphson algorithm as inversion algorithms, respectively.

The 21 000 corresponding combinations of the input image x and the real distribution image y are divided into two groups: a

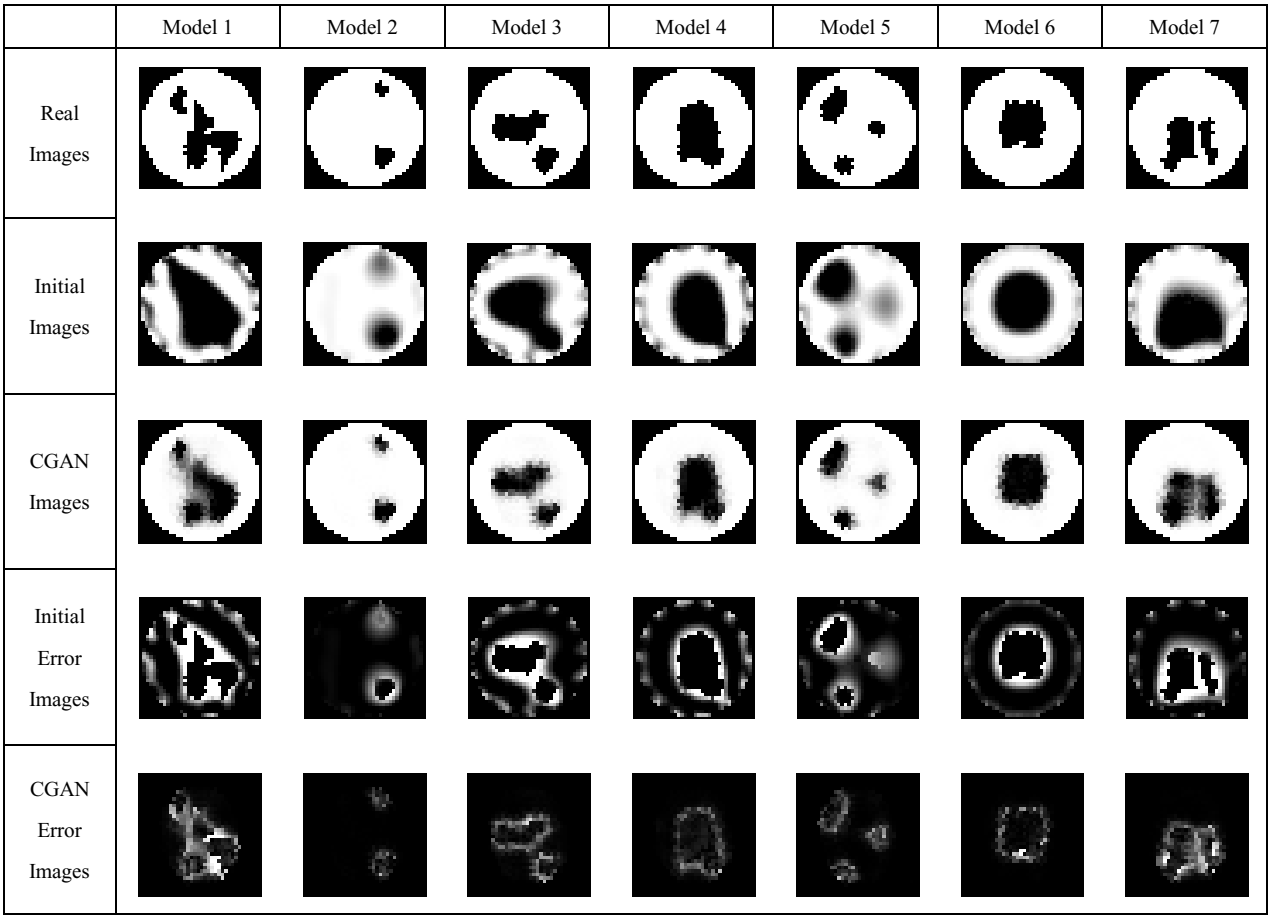

Figure 9. Comparison images of the testing set in which the initial images are reconstructed by using the Landweber algorithm.

training set group and a testing set group. Generally, the size of a testing set is 50% the size of the training set, i.e. the training set group has 14 000 sets, and the testing set group has 7000 sets.

The proposed structure shown in figure 2 is used for training. The initial images are considered as inputs, and the real images are applied as conditions. The training process in this paper is shown in figure 4, where $m = 30, k = 12, n = 100$, and $\mu = 10^{-3}$. The values of m, k, n, and μ are derived from experiments. The 14 000 sets of inputs are divided into 140 batches in the training process. After training is completed, the training results are tested with the testing set, and no duplication exists between the testing set and the training set.

3.2. Evaluation index

The relative image error (RIE) and image correlation coefficient (ICC) are used to evaluate the reconstruction results. A smaller reconstruction error and greater reconstruction correlation mean higher image quality [18].

$$\mathrm{RIE} = \frac{\|\hat{\sigma} - \sigma\|}{\|\sigma\|} \times 100\% \tag{4}$$

$$\mathrm{ICC} = \frac{\sum_{i=1}^{K} (\sigma_i - \bar{\sigma})(\hat{\sigma}_i - \bar{\hat{\sigma}})}{\sqrt{\sum_{i=1}^{K} (\sigma_i - \bar{\sigma})^2 \sum_{i=1}^{K} (\sigma_i - \bar{\hat{\sigma}})^2}}, \tag{5}$$

where $\hat{\sigma}$ is the calculated conductivity distribution, σ is the real conductivity distribution, and $K = 1296$ is the number of pixels in an image.

4. Results and discussion

4.1. Simulation results and analysis

4.1.1. Simulation results. The 7000 initial images in the testing set are input into the generator, and the outputs that are generated are referred to as CGAN images. Seven groups of images are randomly selected from the training set for comparison, as shown in figures 9 and 10. After the initial image is compared with the real image, the absolute value and initial error images are obtained. Similarly, the CGAN error images are obtained. In figure 9, the initial images are reconstructed by using the Landweber algorithm. In figure 10, the initial images are reconstructed by using the Newton–Raphson algorithm.

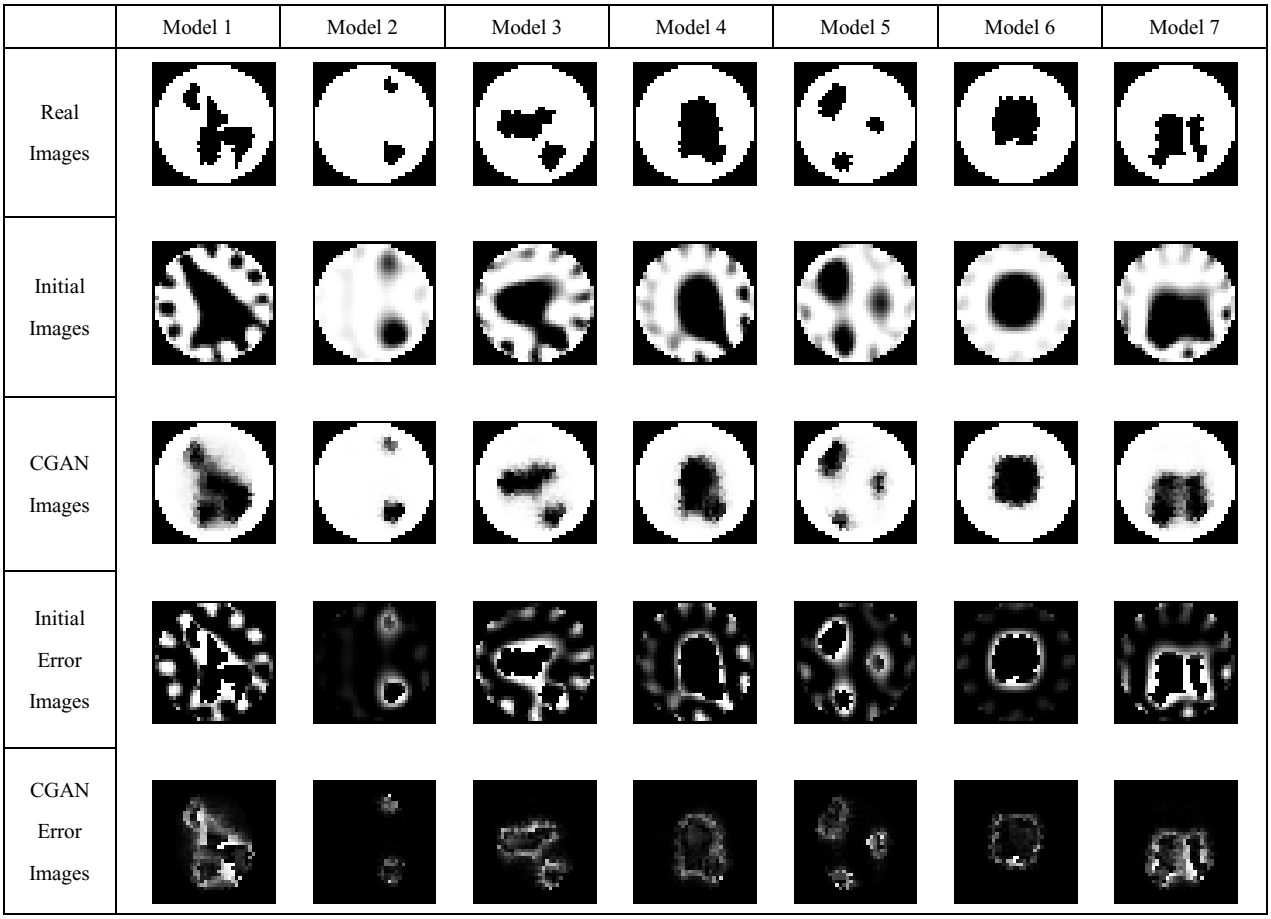

Figure 10. Comparison images of the testing in which the initial images are reconstructed using the Newton–Raphson algorithm.

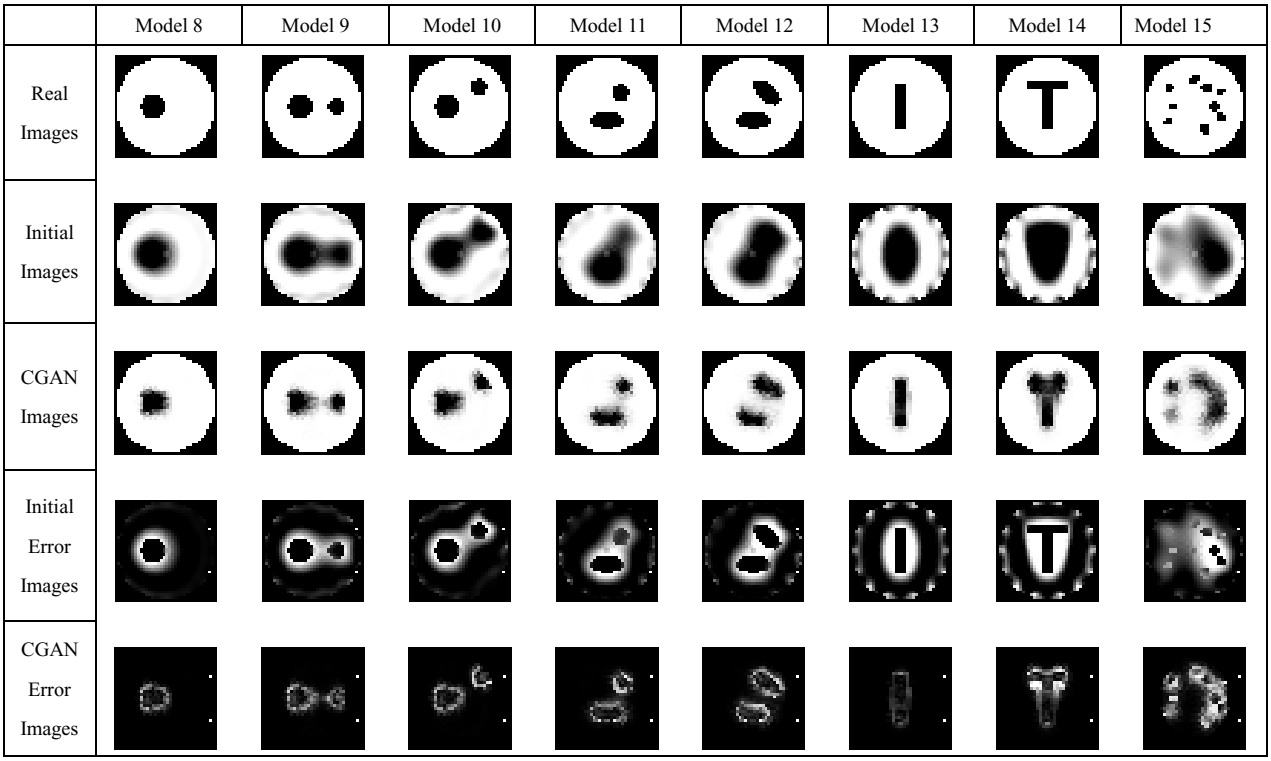

Figure 11. Comparison images of the 8–15 models in which the initial images are reconstructed using the Landweber algorithm.

Table 1. RIE and ICC of reconstructed image of 1–7 models.

	RIE				ICC			
	Landweber		Newton–Raphson		Landweber		Newton–Raphson	
	Initial image	CGAN image	Initial image	CGAN image	Initial image	CGAN image	Initial image	CGAN image
Model 1	23.6393	7.6426	28.6209	8.9137	0.7676	0.9098	0.7189	0.8964
Model 2	3.3100	0.4210	3.0196	0.6177	0.9511	0.9934	0.9560	0.9902
Model 3	16.9246	2.5774	18.0766	2.8743	0.8192	0.9672	0.8066	0.9633
Model 4	12.8364	1.6378	11.1735	1.6570	0.8704	0.9811	0.8855	0.9809
Model 5	9.0551	1.4098	9.1222	2.0330	0.8866	0.9805	0.8893	0.9715
Model 6	9.4575	1.5173	5.3700	1.5835	0.8989	0.9815	0.9399	0.9806
Model 7	16.2394	5.8578	15.6632	5.6722	0.8245	0.9261	0.8324	0.9287

Table 2. RIE and ICC of the 7000 reconstructed images.

	Landweber		Newton–Raphson	
	Initial image	CGAN image	Initial image	CGAN image
RIE_MAX	49.1666	16.6222	55.6213	17.3267
RIE_MIN	0.6609	0.0661	0.6247	0.0516
RIE_Mean	11.9795	2.8045	13.1915	2.9786
ICC_MAX	0.9888	0.9989	0.9895	0.9991
ICC_MIN	0.5032	0.8288	0.4259	0.8068
ICC_Mean	0.8649	0.9639	0.8529	0.9617

Table 3. RIE and ICC of reconstructed image of 8–15 models.

	RIE		ICC	
	Initial image	CGAN image	Initial image	CGAN image
Model 8	6.4264	1.2926	0.9127	0.9802
Model 9	10.9877	2.2292	0.8666	0.9677
Model 10	10.8760	2.6041	0.8674	0.9622
Model 11	10.7775	2.7634	0.8647	0.9596
Model 12	14.8236	3.8746	0.8287	0.9459
Model 13	17.9193	0.6567	0.7854	0.9904
Model 14	23.0505	4.7512	0.7462	0.9349
Model 15	17.5770	8.6907	0.7768	0.8710

To evaluate the performance of the algorithm, models that different from the data generation methods are tested. Considering the Landweber algorithm as an example, models and reconstructed images are shown in figure 11.

4.1.2. Discussion. As shown in the figures 9 and 10, the initial images substantially differ from the real images. However, the CGAN images only slightly differ from the real images, and the errors of the images are substantially reduced. The images reveal that the CGAN algorithm improves the distortion problem in ERT reconstruction. The image reconstructed by the CGAN method performs better in terms of details.

Quantitative analysis of 1–7 models in the testing set is performed. According to (4) and (5) mentioned in section 3.2, RIE and ICC are used to evaluate the CGAN method, as shown in table 1. The algorithm proposed in this paper reduces the error of the image and improves the correlation for the initial image obtained by the two algorithms.

Quantitative analysis of the 7000 testing set is performed, as shown in table 2. The maximum, minimum and mean values of RIE and ICC are listed.

The reconstruction error and correlation analysis of 8–15 models are shown in table 3. The test results prove that the proposed algorithm is effective.

Related parameters of the computer, which are used for training, are listed as follows: CPU: Intel® Core™ i7-5500U, RAM: 8.00 GB, System type: 64-bit operating system. The computer times needed for the different steps of training

Table 4. Computer times needed for the different steps of training (unit of time is seconds).

	Cycle 1	Cycle 2	Cycle 3	Cycle 4	Cycle 5	Cycle 6	Cycle 7	Cycle 8	Cycle 9	Cycle 10	Cycle 11	Cycle 12
Computer times for G	1930.06	2574.16	2562.21	2565.92	2568.8	2569.29	2564.83	2549.02	2532.47	2532.26	2533.77	2533.59
Computer times for D	77.8755	119.206	317.97	3993.79	3986.37	3983.73	3987.45	3955.44	1737.92	1068.43	839.4	

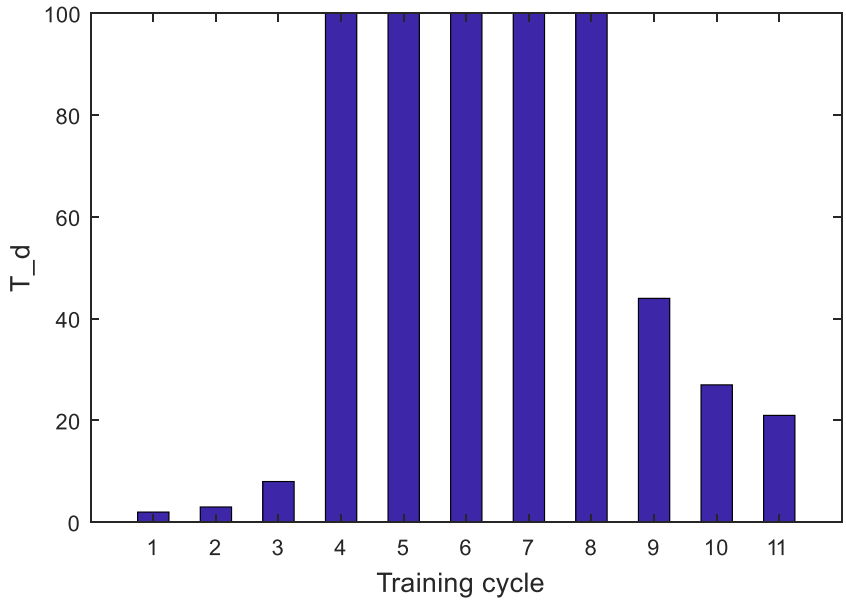

Figure 12. Training times of D during each training cycle.

Figure 13. Experimental setup of the ERT test system.

are shown in table 4. For D, the difference in training time is attributed to the fact that we introduce loss judgements in training.

The training times of D during each training cycle are shown in figure 12. In the first three training cycles, after two, three and eight training times, $L_{\mathrm{CGAN}}(D) < 1.0 \times 10^{-3}$; that is, y and $G(x, z)$ were successfully distinguished. In the 4th to 8th training cycles, after 100 training steps, $L_{\mathrm{CGAN}}(D) < 1.0 \times 10^{-3}$ was impossible to achieve; then, the current training cycle stopped. Subsequently, in the 9th to 11th training cycles, 44, 27 and 21 training times were conducted to achieve $L_{\mathrm{CGAN}}(D) < 1.0 \times 10^{-3}$. A total of 602 training times were conducted in 11 training cycles. The training of introducing error judgement into D can effectively reduce the times of training.

4.2. Experimental results and analysis

An experimental study was conducted to validate the proposed algorithm, as shown in figure 13. This study was developed by the University of Leeds. The configuration of the experimental system is listed below [19].

- Current simulation pattern: adjacent sensing strategy.
- Injected current: 15.10 Ma.
- Current frequency: 9600 Hz.
- Diameter of test field: 50 mm.
- ERT sensor: single-plane 16-electrode sensor.
- Continuous phase material: water.
- Discrete phase material: plexiglass.

The comparison images of the experimental set are shown in figure 14. The CGAN images and the distinction between two discrete phases are clearer. The CGAN method can be employed to reconstruct the sharp corners and edges of an image. The quantitative analysis is shown in table 5. The experiments show that the proposed structure can solve practical problems.

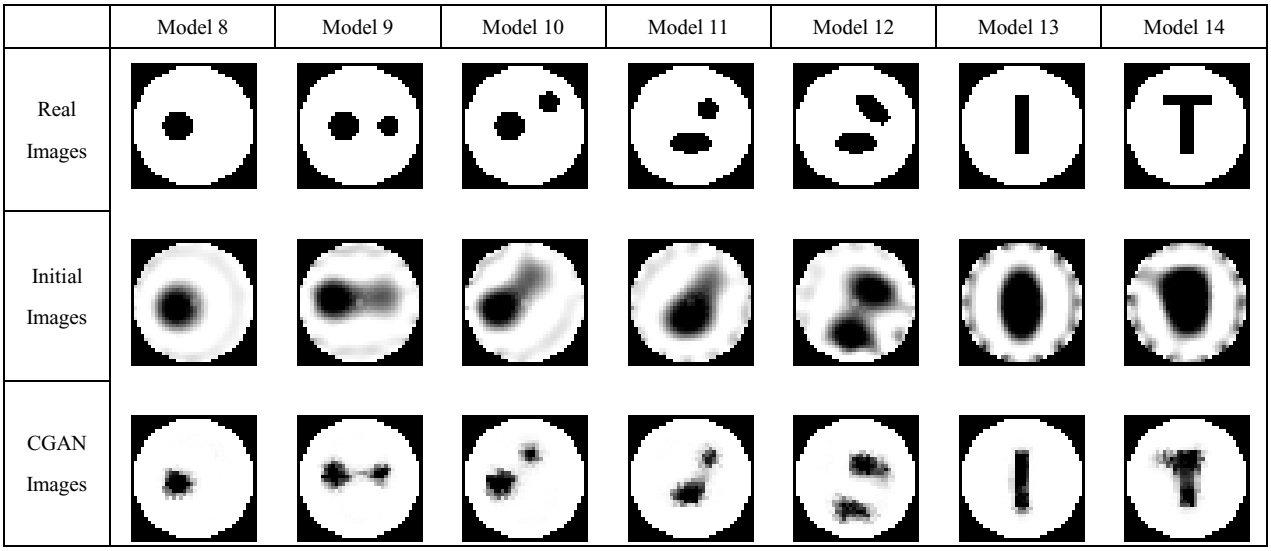

Figure 14. Comparison images of the experimental set.

Table 5. RIE and ICC of the reconstructed image for experimental.

	RIE		ICC	
	Initial image	CGAN image	Initial image	CGAN image
Model 8	4.3447	2.5642	0.9395	0.9604
Model 9	8.5610	7.4329	0.8835	0.8905
Model 10	10.3925	9.4150	0.8535	0.8609
Model 11	8.7027	3.7072	0.8859	0.9455
Model 12	14.5910	9.6118	0.8141	0.8194
Model 13	16.1082	1.1075	0.8056	0.9834
Model 14	18.3022	5.4743	0.7880	0.9218

5. Conclusion

In this paper, a CGAN structure is introduced to ERT reconstruction. The error of the discriminator is used as the basis for setting the training times of the discriminator, and the L1 norm is added to the loss function. In addition, a data generation method that can simulate gas–liquid distribution is proposed.

The simulation shows that images reconstructed by the algorithm mentioned in this paper perform better in terms of details, and the reconstructed images are more accurate. Experiments show that this method can solve practical problems. The sharp corners and edges of the reconstructed image are clear.

In the future, additional research should be conducted. The coverage of the dataset should be expanded to the real distribution and its accuracy should be improved. In addition, the impact of different deep learning structures on reconstruction deserves further study.

ORCID iDs

Yutong Chen https://orcid.org/0000-0001-8137-444X
Kun Li https://orcid.org/0000-0002-4439-7586

References

[1] Dickin F and Wang M 1996 Electrical resistance tomography for process applications *Meas. Sci. Technol.* **7** 247–60
[2] Geselowitz D B 1971 An application of electrocardiographic lead theory to impedance plethysmography *IEEE Trans. Biomed. Eng.* **BME-18** 38–41
[3] Na W, Jia J, Yu X, Faraj Y, Wang Q, Meng Y-F, Wang M and Sun W 2015 Imaging of gas–liquid annular flows for underbalanced drilling using electrical resistance tomography *Flow Meas. Instrum.* **46** 319–26
[4] Madd R, Hou R and Martin P 2016 Biofilm disruption of Bacillus subtilis BBK006 by biosurfactants using electrical resistance tomography (ERT) *New Biotechnol.* **33** S120
[5] Kotre C J 1994 EIT image reconstruction using sensitivity weighted filtered backprojection *Physiol. Meas.* **15.2A** A125–36
[6] Peng L H, Merkus H and Scarlett B 2000 Using regularization methods for image reconstruction of electrical capacitance tomography *Part. Part. Syst. Charact.* **17** 96–104
[7] Kim C Y *et al* 2012 Modified newton-raphson method using a region of interest in electrical impedance tomography *J. Korean Phys. Soc.* **61** 1199–205
[8] Yan H, Wang Y and Zhou Y 2014 Three-dimensional electrical capacitance tomography reconstruction by the Landweber iterative algorithm with fuzzy thresholding *Sci. Meas. Technol.* **8** 487–96
[9] Zheng J and Peng L 2018 An autoencoder-based image reconstruction for electrical capacitance tomography *IEEE Sens. J.* **18** 5464–74
[10] Hamilton S J and Hauptmann A 2017 Deep D-bar: real-time electrical impedance tomography imaging with deep neural networks *IEEE Trans. Med. Imaging* **37** 2367–77

[11] Tan C *et al* 2018 Image reconstruction based on convolutional neural network for electrical resistance tomography *IEEE Sens. J.* **19** 196–204
[12] Xiao J *et al* 2018 Deep learning image reconstruction simulation for electromagnetic tomography *IEEE Sens. J.* **18** 3290–8
[13] Lei J, Liu Q and Wang X 2018 Deep learning-based inversion method for imaging problems in electrical capacitance tomography *IEEE Trans. Instrum. Meas.* **67** 2107–18
[14] Mirza M and Osindero S 2014 Conditional generative adversarial nets *Comput. Sci.* 2672–80 (arXiv:1406.2661)
[15] Isola P *et al* 2016 Image-to-image translation with conditional adversarial networks (arXiv:1611.07004)
[16] Zhao L *et al* 2017 Simultaneously color-depth super-resolution with conditional generative adversarial network *Pattern Recognit.* (arXiv:1708.09105)
[17] Wang Y *et al* 2018 3D conditional generative adversarial networks for high-quality PET image estimation at low dose *NeuroImage* **174** 550–62
[18] Yang W Q *et al* 1999 An image-reconstruction algorithm based on Landweber's iteration method for electrical-capacitance tomography *Meas. Sci. Technol.* **10** 1065–9
[19] Brown B H and Seagar A D 1985 Applied potential tomography: data collection problems *IEE Int. Conf. on Electric and Magnetic fields in Medicine and Biology (London, December)* p 79e82